Check for updates

Calcium carbonate dissolution patterns in the ocean

Olivier Sulpis [1]✉, Emil Jeansson [2], Ashley Dinauer[3], Siv K. Lauvset [2] and Jack J. Middelburg [1]

Calcium carbonate ($CaCO_3$) minerals secreted by marine organisms are abundant in the ocean. These particles settle and the majority dissolves in deeper waters or at the seafloor. Dissolution of carbonates buffers the ocean, but the vertical and regional distribution and magnitude of dissolution are unclear. Here we use seawater chemistry and age data to derive pelagic $CaCO_3$ dissolution rates in major oceanic regions and provide the first data-based, regional profiles of $CaCO_3$ settling fluxes. We find that global $CaCO_3$ export at 300 m depth is 76 ± 12 Tmol yr^{-1}, of which 36 ± 8 Tmol (47%) dissolves in the water column. Dissolution occurs in two distinct depth zones. In shallow waters, metabolic CO_2 release and high-magnesium calcites dominate dissolution while increased $CaCO_3$ solubility governs dissolution in deeper waters. Based on reconstructed sinking fluxes, our data indicate a higher $CaCO_3$ transfer efficiency from the surface to the seafloor in high-productivity, upwelling areas than in oligotrophic systems. These results have implications for assessments of future ocean acidification as well as palaeorecord interpretations, as they demonstrate that surface ecosystems, not only interior ocean chemistry, are key to controlling the dissolution of settling $CaCO_3$ particles.

I n the open surface ocean, coccolithophores, foraminifera and pteropods are common planktonic groups producing calcium carbonate ($CaCO_3$) shells or skeletons. These biominerals are exported from the surface ocean following different pathways, including being incorporated into other biogenic particles such as marine snow aggregates and faecal pellets[1,2]. The exported $CaCO_3$ particles are redistributed over the water column, with a fraction reaching the seafloor. At the seafloor, $CaCO_3$ dissolution is the ultimate sink of anthropogenic CO_2 on multimillennial timescales[3]. Quantifying the current marine $CaCO_3$ sources and sinks, and how they vary geographically, is thus a requirement to predict future ocean acidification. Yet the exact nature, magnitude and distribution of marine $CaCO_3$ settling and dissolution fluxes remain undetermined.

Marine $CaCO_3$ is found in the form of calcite, aragonite and magnesium (Mg) calcites (Fig. 1). Calcite, the most stable polymorph under Earth surface conditions, constitutes the shells of most coccolithophores and planktonic foraminifera. Aragonite, more soluble than pure calcite, mostly makes up the skeletons of pteropods. Biogenic Mg calcites, whose Mg content exceeds 10–15 mol% and whose solubility can be twice as large as that of aragonite[4], are ubiquitous in shallow environments, constituting the skeletons and shells of red coralline algae, benthic foraminifera and bryozoans, among others[5]. In the open ocean, Mg calcites are secreted by fish—which could account for up to 15% of total $CaCO_3$ production[6]—and imported from shallow shelves and banks[7,8]. Thus, although most studies treat the settling pool of $CaCO_3$ particles as consisting of pure calcite, aragonite and Mg calcites could represent a substantial fraction of the total $CaCO_3$ rain[6,9,10] and be the first responders to ocean acidification[11]. Direct observations of the settling flux of particles and their properties are still very sparse and primarily based on sediment-trap measurements subject to well-known collection biases[12]. As a consequence, global estimates of surface $CaCO_3$ export found in the literature span a very wide

range from ~50 Tmol yr^{-1} (refs. [13,14]) to over 130 Tmol yr^{-1} (refs. [15,16]) (for a literature review, see Supplementary Fig. 1). How the settling flux of exported $CaCO_3$ varies regionally and with depth is unknown. Irrespectively, the $CaCO_3$ flux to the seafloor is relatively well known, with recent studies[15,17,18] suggesting that between 40 and 60 Tmol $CaCO_3$ (Fig. 1) settle to the seafloor each year.

The degree of saturation of seawater with respect to each $CaCO_3$ mineral is the driving force behind its precipitation or dissolution[19]. While the surface ocean is currently supersaturated with respect to both calcite and aragonite[20], cold deep waters are typically undersaturated with respect to both minerals[21,22], mainly because the solubility of these minerals increases with increasing seawater depth/pressure[23] and because of the increase in dissolved inorganic carbon relative to total alkalinity in the deep ocean. The depths at which undersaturation with respect to calcite, aragonite or Mg calcites first occurs are termed the calcite, aragonite and Mg-calcite saturation depths (Fig. 1). Note that there is a range of Mg calcites in the ocean, each with a given Mg content, solubility and saturation depth[24]. Here, for simplicity, we use toadfish Mg calcite as a surrogate for a typical oceanic Mg-calcite mineral, using a solubility product for toadfish Mg calcite from ref. [4]. The associated globally averaged Mg-calcite saturation depth is 333 ± 210 m, leaving 90% of the ocean volume undersaturated with respect to this particular mineral.

Since $CaCO_3$ dissolution occurs slowly in the marine environment, direct in situ measurements of its rate are extremely scarce, and their spatial coverage is very sparse[21,22,25,26]. Hence, the location and magnitude of water-column dissolution of $CaCO_3$ are still subject to considerable debate. Seawater undersaturated with respect to $CaCO_3$ minerals is not confined exclusively to depths below their saturation depths, but can be found in shallow microenvironments locally acidified by CO_2 released during organic matter degradation, such as zooplankton and fish guts[27] and settling zooplankton faecal pellets or bodies of $CaCO_3$ producers[28] (Fig. 1). High $CaCO_3$

[1]Earth Sciences, Utrecht University, Utrecht, The Netherlands. [2]NORCE Norwegian Research Centre, Bjerknes Centre for Climate Research, Bergen, Norway. [3]Climate and Environmental Physics, Physics Institute and Oeschger Centre for Climate Change Research, University of Bern, Bern, Switzerland. ✉e-mail: o.j.t.sulpis@uu.nl
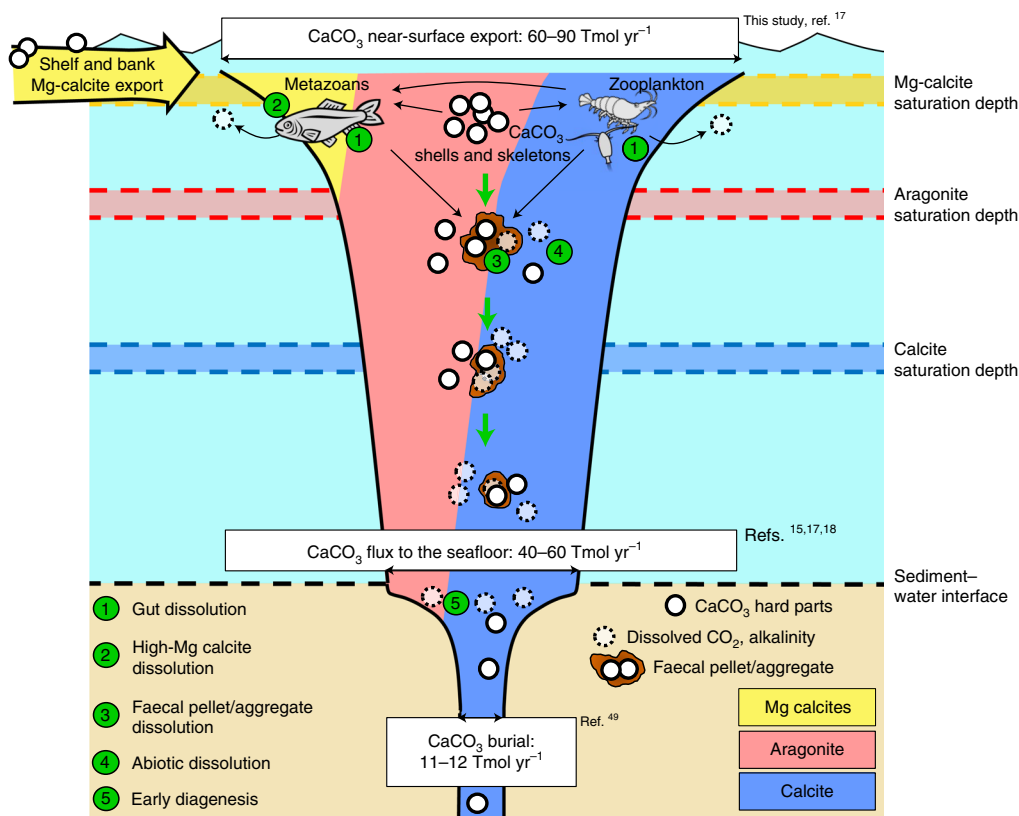
Fig. 1 | Conceptual view of the oceanic CaCO₃ cycle. Fluxes given in Tmol yr⁻¹ are the CaCO₃ export flux from the surface ocean, the CaCO₃ flux reaching the seafloor and the CaCO₃ flux buried in sediments. Green circles indicate the five main mechanisms of dissolution.

dissolution rates in the top kilometre have been suggested to be ubiquitous[29–32] and are supported by the presence of excess alkalinity and excess calcium[29–33], etching of CaCO₃ surfaces[34,35] and decreased sinking fluxes of CaCO₃ measured by upper-ocean sediment traps[25,36]. While shallow-water dissolution is in contradiction to the traditional pattern of CaCO₃ particles sinking unaffected through the upper ocean, dissolving only once their saturation depth is crossed[37], two possible mechanisms could explain it: metabolic CO₂ production creating acidic microenvironments or dissolution of more-soluble CaCO₃ phases such as aragonite or Mg calcites[9,11]. However, the relative importance of biologically mediated CaCO₃ dissolution is still controversial[38], and many basic questions, such as which CaCO₃ polymorphs are dissolving and what the controlling factors are, remain unanswered.

Given that the nature, magnitude and distribution of the surface export of CaCO₃ are poorly constrained, and that the driving mechanisms behind dissolution in the water column are difficult to unravel, top-down calculations involving CaCO₃ export fluxes are unlikely to yield accurate assessments of CaCO₃ settling and dissolution fluxes. In this study, we employ an alternative bottom-up approach to calculate regional settling fluxes of CaCO₃ by combining CaCO₃ fluxes at the seafloor[18,39,40] with estimates of pelagic (water column) CaCO₃ dissolution based on seawater alkalinity and age observations (Methods and Extended Data Figs. 1–6). In a wide range of oceanic regions, we plot excess alkalinity (the alkalinity increase corrected for metabolism) against seawater age along predefined isopycnals and extract the slope of this relationship to obtain the total CaCO₃ dissolution rate[15,29–32] (r_{CaCO_3}; Methods). Vertical profiles of the CaCO₃ settling flux (F_{CaCO_3}) are then reconstructed by integrating r_{CaCO_3} over each depth level, starting from the deepest. The bottommost F_{CaCO_3} is taken from the sum of the CaCO₃

burial rate in the sediments and the CaCO₃ dissolution rate at the sediment–water interface[18,39,40]. We find that most marine CaCO₃ dissolution occurs in two distinct depth realms of the ocean: (1) in the top kilometre of the ocean (mainly above the aragonite and calcite saturation depths) and (2) at the seafloor. While dissolution at the seafloor is driven mainly by undersaturated bottom waters, dissolution in the top kilometre is ecosystem-specific, supposedly driven primarily by CO₂ released from microbial and/or animal respiration and/or by the presence of highly soluble Mg calcites.

Two distinct dissolution regimes for settling CaCO₃

In all oceanic regions (Extended Data Fig. 2), vertical profiles of r_{CaCO_3} exhibit a similar pattern: high rates of dissolution occur near the surface and rates are strongly attenuated with depth in the top kilometre, increasing again in deeper waters (Fig. 2). These two distinct dissolution regimes, separated with black arrows in Fig. 2, differ in terms of driving forces: while metabolic processes and the presence of Mg calcites control shallow-water dissolution, the higher solubility of CaCO₃ in bulk solution at depth is responsible for dissolution in deeper waters.

The fact that there is a strong attenuation of the settling flux of CaCO₃ with depth, as with the sinking particulate organic carbon flux, insinuates that they are linked and governed by similar processes involving microbial and metazoan consumers. Upper-kilometre CaCO₃ dissolution rates are highest in the subtropical gyre regions of the Pacific, Atlantic and Indian oceans and increase with increasing oxygen utilization rates (Supplementary Fig. 2), suggesting that subtropical regions are hotspots of respiration-driven CaCO₃ dissolution. Although biological productivity and carbon export are low in subtropical gyres[13], the dominance of coccolithophores, which are well adapted to nutrient-poor, low-turbulence regimes, could
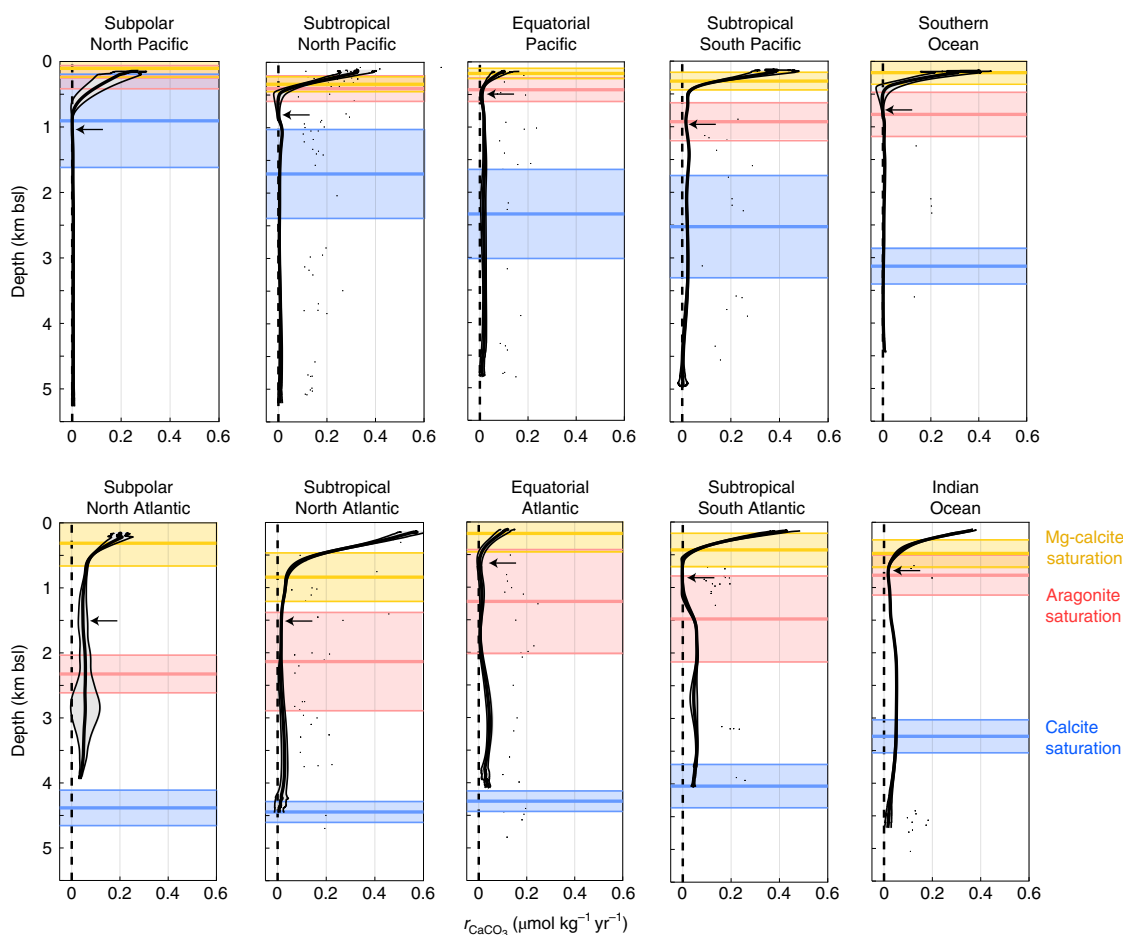
Fig. 2 | Regional profiles of reconstructed CaCO₃ dissolution rates and saturation horizons. In each panel, the central black line is the reconstructed regional mean total CaCO₃ dissolution rate, and the grey envelope represents the 90% confidence interval, accounting for the regional variability and uncertainties associated with the seawater chemistry and age estimates. The regional mean Mg-calcite (yellow), aragonite (red) and calcite (blue) saturation depths are represented with their uncertainty envelopes (1σ). Black arrows mark the depth limit between the upper dissolution regime, driven by CO_2 produced during microbial and/or animal respiration and by the presence of highly soluble Mg calcites, and the lower dissolution regime, driven by increased CaCO₃ solubility in bulk solution at high pressure. This depth limit is computed as the shallowest depth at which the depth derivative of the vertical dissolution rate profile is equal to zero. bsl, below sea level.

explain higher CaCO₃ dissolution in the top kilometre of subtropical gyre regions. Coccolithophores, on their own, settle through the water column very slowly[41] and have high CaCO₃-reactive surface areas[42], creating a very high potential for biologically mediated dissolution above the calcite saturation depth. By contrast, the highly productive equatorial Pacific and Atlantic regions, hotspots of carbon export[13], show the lowest upper-kilometre CaCO₃ dissolution rates.

In all regions, r_{CaCO_3} profiles reveal a second deeper, smaller maximum (Fig. 2). The onset of this deeper CaCO₃ dissolution lies at the aragonite saturation depth in most regions, except for the North Pacific and the subpolar North Atlantic. This implies that aragonite, not calcite, is the polymorph dominating pelagic dissolution in the deep ocean. The important role of aragonite is consistent with (1) recent model studies suggesting that a substantial fraction of exported CaCO₃ may be aragonite[9,10], (2) in situ observations of pteropod dissolution[28,36,43] and (3) recent sediment-trap data showing high amounts of pteropod genetic material[44] and aragonite at abyssal depths[25].

The dissolution rates shown in Fig. 2 are much lower than those shown in ref. [32]; that is, they are lower by about 0.5 µmol kg⁻¹ over the entire water column. The latter estimates are too high to fit within published marine CaCO₃ budgets as demonstrated in ref. [38]

and in the Supplementary Information. We attribute part of this discrepancy to differences in seawater age estimates, as this work uses a transit time distribution (TTD) approach[45], whereas in the earlier work[29–32] ages were derived from a direct comparison between seawater and atmospheric chlorofluorocarbon (CFC) concentrations. This 'traditional' CFC-age (or 'tracer age') method neglects mixing that occurs during the transport of a water parcel into the ocean interior, with the consequence that apparent seawater ages are underestimated (Supplementary Fig. 1) and resulting CaCO₃ dissolution rates are overestimated. By contrast, the TTD approach used here keeps track of seawater mixing history by including corrections for mixing during transport away from the surface. More details on the TTD method and its limitations are included in the Supplementary Information.

Reconstructed CaCO₃ export and sinks
Reconstructed F_{CaCO_3} decreases with depth in all oceanic regions (Fig. 3). In regions where near-surface dissolution is strong, such as the subtropical regions, a sharp F_{CaCO_3} decrease occurs in the top kilometre. The fraction of CaCO₃ export reaching the seafloor (transfer efficiency) is high in upwelling regions such as the Southern Ocean, subpolar North Pacific and equatorial Pacific ($86 \pm 34\%$ on average for these three regions), where the extent of pelagic CaCO₃
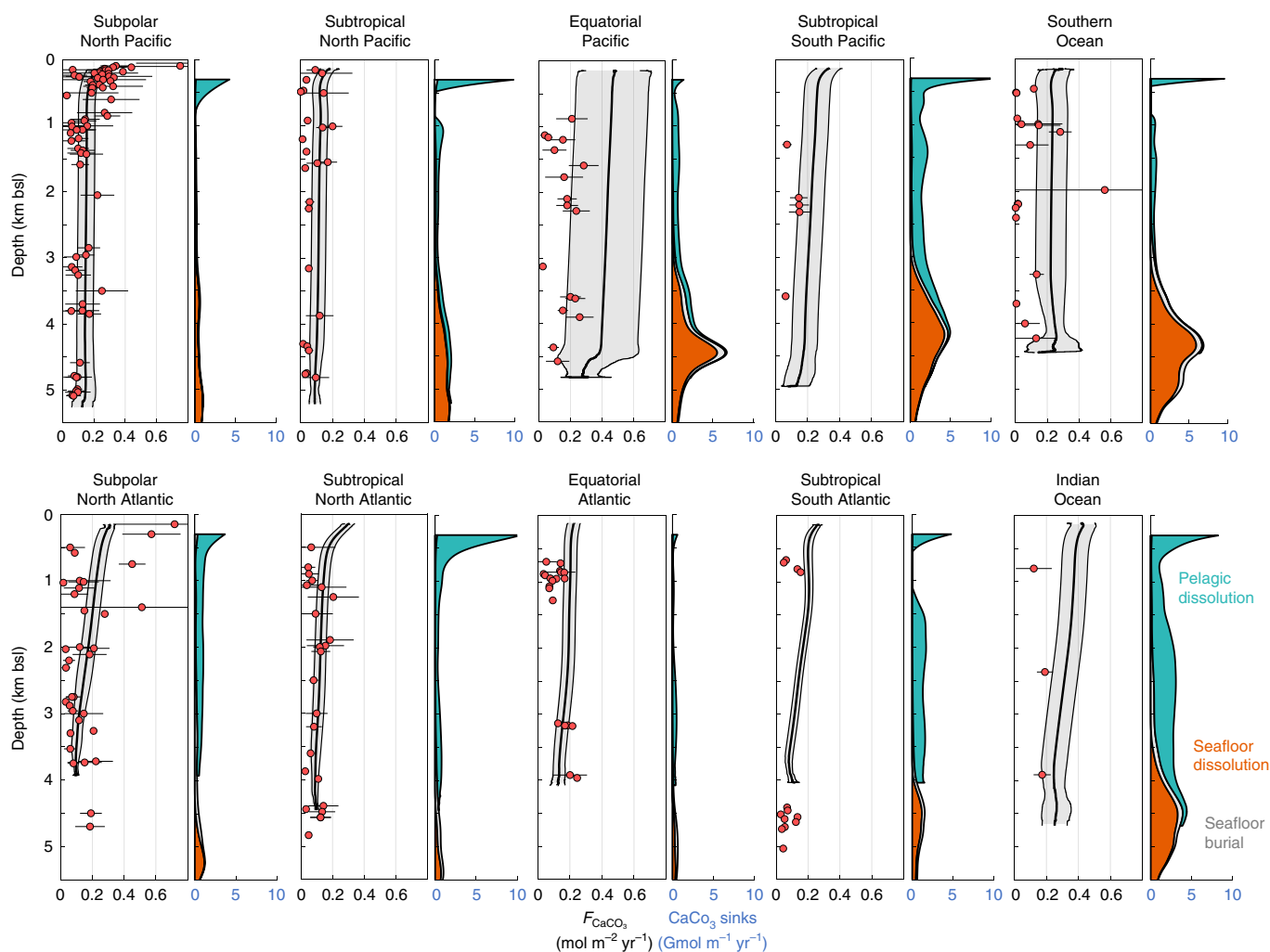
Fig. 3 | Reconstructed regional CaCO₃ settling fluxes and depth distributions of their sinks. For each oceanic region, the central black line in the left panel is the reconstructed regional mean F_{CaCO_3} (mol m⁻² yr⁻¹), and the grey envelope represents the 90% confidence interval, accounting for the regional variability and uncertainties associated with the seawater chemistry and age estimates. Red dots are CaCO₃ settling fluxes measured by sediment traps. Horizontal error bars associated with sediment-trap measurements represent the spatial and temporal variability of measurements originating from the same region and depth (1σ). For each region, the right panel shows the horizontally integrated CaCO₃ dissolution in the water column in turquoise, dissolution at the sediment–water interface in orange and burial in the sediments in grey (CaCO₃ sinks, Gmol m⁻¹ yr⁻¹).

dissolution is limited (Figs. 2 and 3). This high CaCO₃ transfer efficiency could be explained by the higher export of rapidly sinking pteropods in high-latitude regions[46,47] and/or by the presence of diatoms. Diatom-dominated regions, generally of high resources and turbulence, tend to correspond to regions of rapidly sinking aggregates due to the large production of transparent exopolymer particles by diatoms that act as glue and drive the aggregation process[47]. Rapidly sinking particles leave less time for the particulate organic carbon and CaCO₃ they contain to be remineralized/dissolved in the water column. The lowest transfer efficiency is found in the subtropical North and South Atlantic (27 ± 13% in average for these two regions), where coccolithophores probably dominate surface productivity and where settling CaCO₃ particles are subject to intense dissolution in the top kilometre and beneath the aragonite saturation depth (Fig. 2).

The vertical extents of r_{CaCO_3} and F_{CaCO_3} profiles (Figs. 2 and 3) are limited by the availability of seawater excess alkalinity and age data, often scarce in near-bottom waters. In addition, part of the excess alkalinity buildup in the surface ocean could derive from vertical diffusion from deeper waters[38], although the shapes

of titration alakalinity (TA) depth gradients across regions suggest that vertical transport could also lead to TA removal from the upper layer (Supplementary Information). Nonetheless, the reconstructed regional profiles of F_{CaCO_3} are broadly consistent with the range of CaCO₃ fluxes measured by sediment traps (red circles in Fig. 3). Integrating over the global surface area of the ocean, we obtain a global total CaCO₃ flux at 300 m of 76 ± 12 Tmol yr⁻¹ (Fig. 4a), which is within the wide range of previous estimates of globally integrated CaCO₃ export (~50 to ~150 Tmol yr⁻¹, Supplementary Fig. 1)[13–16] and within the uncertainty range (60–87.5 Tmol yr⁻¹) of ref. [17]. The global total pelagic CaCO₃ dissolution rate (36 ± 8 Tmol yr⁻¹, Fig. 4b) is consistent with estimates from the literature (between ~25 and ~85 Tmol yr⁻¹)[17,32,48] and implies that globally integrated pelagic CaCO₃ dissolution is on par with CaCO₃ burial (10 ± 2 Tmol yr⁻¹) and dissolution (30 ± 6 Tmol yr⁻¹) at the sediment–water interface[15,18,49].

We also compared our reconstructed profile of the global horizontally integrated F_{CaCO_3} with that predicted by the historical simulation of the Institut Pierre Simon Laplace (IPSL) CM6A-LR climate model averaged from 1985 to 2014[50,51] (Fig. 4a). This model uses the PISCES-v2 biogeochemical module[52], which represents
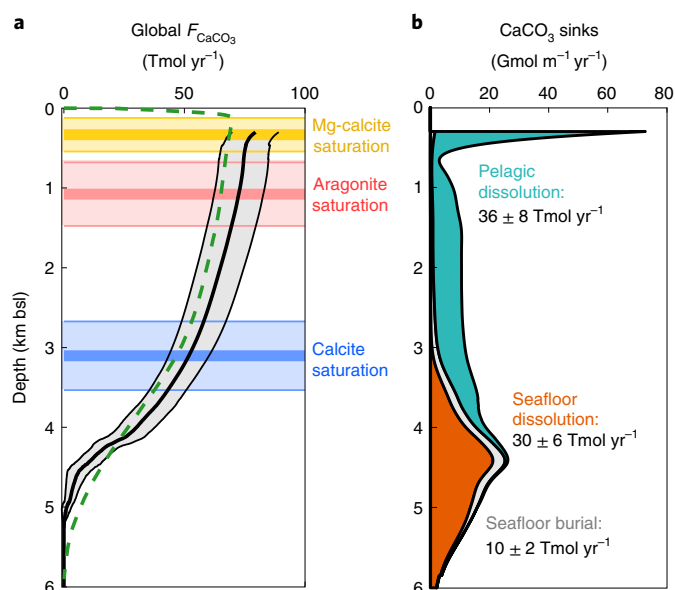
Fig. 4 | Global CaCO₃ settling flux profile and depth distribution of its sinks. a, The central black line is the global horizontally integrated reconstructed F_{CaCO_3}, and the grey envelope represents the 90% confidence interval, accounting for the regional variability and uncertainties associated with the seawater chemistry and age estimates. The globally averaged Mg-calcite, aragonite and calcite saturation depths are represented by the yellow, red and blue horizontal lines, respectively, with 1σ uncertainty envelopes. The dark-green dashed line is the global horizontally integrated F_{CaCO_3} predicted by the historical simulation of the IPSL-CM6A-LR Earth system model, averaged from 1985 to 2014. **b,** Global horizontally integrated CaCO₃ dissolution in the water column (turquoise), dissolution at the sediment–water interface (orange) and burial in the sediments (grey).

calcite dissolution in zooplankton guts and in deeper, undersaturated waters, but it does not include aragonite or Mg calcites. The calcite sinking flux predicted by the IPSL model is on the lower end of our reconstructed F_{CaCO_3} over the entire water column (Fig. 4a), although the difference between them ($8 \pm 12 \, \text{Tmol yr}^{-1}$ at 300 m depth) is not substantial. This suggests that metabolic processes may be more important than the presence of aragonite and Mg calcites in explaining the amount of CaCO₃ dissolved in the water column and the pattern of dissolution. Our estimate for pelagic dissolution above the calcite saturation depth is $29 \pm 6 \, \text{Tmol yr}^{-1}$. Accordingly, the lower bound for pelagic dissolution of calcite due to respiration-derived CO₂ can be calculated by difference as $(29 - 8 =) 21 \pm 13 \, \text{Tmol yr}^{-1}$. In other words, at least $58 \pm 38\%$ of the CaCO₃ that dissolves in the water column per year could be in the form of calcite and driven by metabolic CO₂.

Our results provide data-based, regional profiles of CaCO₃ settling fluxes and indicate that surface-ocean ecosystems are key to determining their magnitude and depth distributions. Most CaCO₃ dissolution occurs in two distinct regions of the water column: in the top kilometre (at least $9 \pm 3 \, \text{Tmol yr}^{-1}$) and at the seafloor ($30 \pm 6 \, \text{Tmol yr}^{-1}$). Yet, factors governing CaCO₃ dissolution and its sensitivity to anthropogenic CO₂ differ between these two depth realms. Dissolution in shallow waters can be attributed to dissolution of highly soluble Mg calcites and/or to metabolic CO₂ production within marine organisms or aggregates—although we cannot quantify the relative contribution of each—while dissolution near the sediment surface depends primarily on bottom-water chemistry. Projections of shallowing aragonite and calcite saturation depths as anthropogenic CO₂ penetrates into the ocean[53,54] may

not necessarily lead to increased overall pelagic CaCO₃ dissolution because dissolution in the top kilometre is constrained to a large extent by metabolic activities and high Mg-calcite dissolution. Shallow dissolution depends strongly on ecosystem functioning, for example, the ratio of CaCO₃ to particulate organic carbon in the continuous rain of sinking biogenic particles (rain ratio[55]) and the relative proportions of high Mg calcites, aragonite and calcite in settling fluxes (community composition). Any perturbation in food web structure due to ocean acidification, warming or fertilization thus impacts dissolution on much shorter timescales than those related to deep-water dissolution.

Online content

Any methods, additional references, Nature Research reporting summaries, source data, extended data, supplementary information, acknowledgements, peer review information; details of author contributions and competing interests; and statements of data and code availability are available at https://doi.org/10.1038/s41561-021-00743-y.

References
1. Richardson, T. L. Mechanisms and pathways of small-phytoplankton export from the surface ocean. *Annu. Rev. Mar. Sci.* **11**, 57–74 (2019).
2. Silver, M. W., Shanks, A. L. & Trent, J. D. Marine snow: microplankton habitat and source of small-scale patchiness in pelagic populations. *Science* **201**, 371–373 (1978).
3. Archer, D. et al. Atmospheric lifetime of fossil fuel carbon dioxide. *Annu. Rev. Earth Planet. Sci.* **37**, 117–134 (2009).
4. Woosley, R. J., Millero, F. J. & Grosell, M. The solubility of fish-produced high magnesium calcite in seawater. *J. Geophys. Res. Oceans* **117**, C04018 (2012).
5. Chave, K. E. Aspects of the biogeochemistry of magnesium 1. Calcareous marine organisms. *J. Geol.* **62**, 266–283 (1954).
6. Wilson, R. W. et al. Contribution of fish to the marine inorganic carbon cycle. *Science* **323**, 359–362 (2009).
7. Berner, R. A., Berner, E. K. & Keir, R. S. Aragonite dissolution on the Bermuda Pedestal: its depth and geochemical significance. *Earth Planet. Sci. Lett.* **30**, 169–178 (1976).
8. Agegian, C. R., Mackenzie, F. T., Tribble, J. S. & Sabine, C. L. in *Biogeochemical Cycling and Fluxes Between the Deep Euphotic Zone and Other Oceanic Realms* (ed. Agegian, C. R.) 5–32 (Undersea Research Program, National Oceanic and Atmospheric Administration, 1988).
9. Buitenhuis, E. T., Le Quéré, C., Bednaršek, N. & Schiebel, R. Large contribution of pteropods to shallow CaCO₃ export. *Glob. Biogeochem. Cycles* **33**, 458–468 (2019).
10. Gangstø, R. et al. Modeling the marine aragonite cycle: changes under rising carbon dioxide and its role in shallow water CaCO₃ dissolution. *Biogeosciences* **5**, 1057–1072 (2008).
11. Morse, J. W., Andersson, A. J. & Mackenzie, F. T. Initial responses of carbonate-rich shelf sediments to rising atmospheric pCO₂ and "ocean acidification": role of high Mg-calcites. *Geochim. Cosmochim. Acta* **70**, 5814–5830 (2006).
12. Buesseler, K. O. et al. An assessment of the use of sediment traps for estimating upper ocean particle fluxes. *J. Mar. Res.* **65**, 345–416 (2007).
13. Dunne, J. P., Sarmiento, J. L. & Gnanadesikan, A. A synthesis of global particle export from the surface ocean and cycling through the ocean interior and on the seafloor. *Glob. Biogeochem. Cycles* https://doi.org/10.1029/2006gb002907 (2007).
14. Milliman, J. D. Production and accumulation of calcium carbonate in the ocean: budget of a nonsteady state. *Glob. Biogeochem. Cycles* **7**, 927–957 (1993).
15. Berelson, W. M. et al. Relating estimates of CaCO₃ production, export, and dissolution in the water column to measurements of CaCO₃ rain into sediment traps and dissolution on the sea floor: a revised global carbonate budget. *Glob. Biogeochem. Cycles* https://doi.org/10.1029/2006gb002803 (2007).
16. Smith, S. V. & Mackenzie, F. T. The role of CaCO₃ reactions in the contemporary oceanic CO₂ cycle. *Aquat. Geochem.* https://doi.org/10.1007/s10498-015-9282-y (2016).
17. Battaglia, G., Steinacher, M. & Joos, F. A probabilistic assessment of calcium carbonate export and dissolution in the modern ocean. *Biogeosciences* **13**, 2823–2848 (2016).

18. Sulpis, O. et al. Current CaCO₃ dissolution at the seafloor caused by anthropogenic CO₂. *Proc. Natl Acad. Sci. USA* **115**, 11700–11705 (2018).
19. Mucci, A. The solubility of calcite and aragonite in seawater at various salinities, temperatures and one atmosphere total pressure. *Am. J. Sci.* **283**, 780–799 (1983).
20. Hoegh-Guldberg, O. et al. Coral reefs under rapid climate change and ocean acidification. *Science* **318**, 1737–1742 (2007).
21. Peterson, M. N. A. Calcite: rates of dissolution in a vertical profile in the Central Pacific. *Science* **154**, 1542–1544 (1966).
22. Berger, W. H. Foraminiferal ooze: solution at depths. *Science* **156**, 383–385 (1967).
23. Millero, F. J. The thermodynamics of the carbonic acid system in seawater. *Geochim. Cosmochim. Acta* **43**, 1651–1661 (1979).
24. Morse, J. W. & Mackenzie, F. T. *Geochemistry of Sedimentary Carbonates* (Elsevier, 1990).
25. Dong, S. et al. Aragonite dissolution kinetics and calcite/aragonite ratios in sinking and suspended particles in the North Pacific. *Earth Planet. Sci. Lett.* **515**, 1–12 (2019).
26. Honjo, S. & Erez, J. Dissolution rates of calcium carbonate in the deep ocean; an in-situ experiment in the North Atlantic Ocean. *Earth Planet. Sci. Lett.* **40**, 287–300 (1978).
27. White, M. M. et al. Coccolith dissolution within copepod guts affects fecal pellet density and sinking rate. *Sci. Rep.* **8**, 9758 (2018).
28. Oakes, R. L., Peck, V. L., Manno, C. & Bralower, T. J. Degradation of internal organic matter is the main control on pteropod shell dissolution after death. *Glob. Biogeochem. Cycles* **33**, 749–760 (2019).
29. Feely, R. A. et al. In situ calcium carbonate dissolution in the Pacific Ocean. *Glob. Biogeochem. Cycles* https://doi.org/10.1029/2002gb001866 (2002).
30. Sabine, C. L., Key, R. M., Feely, R. A. & Greeley, D. Inorganic carbon in the Indian Ocean: distribution and dissolution processes. *Glob. Biogeochem. Cycles* **16**, 15-11–15-18 (2002).
31. Chung, S. N. et al. Calcium carbonate budget in the Atlantic Ocean based on water column inorganic carbon chemistry. *Glob. Biogeochem. Cycles* https://doi.org/10.1029/2002gb002001 (2003).
32. Feely, R. A. et al. Impact of anthropogenic CO₂ on the CaCO₃ system in the oceans. *Science* **305**, 362–366 (2004).
33. Rosón, G., Guallart, E. F., Pérez, F. F. & Ríos, A. F. Calcium distribution in the subtropical Atlantic Ocean: implications for calcium excess and saturation horizons. *J. Mar. Syst.* **158**, 45–51 (2016).
34. Andruleit, H. A. Dissolution-affected coccolithophore fluxes in the central Greenland Sea (1994/1995). *Deep Sea Res. II* **47**, 1719–1742 (2000).
35. Troy, P. J., Li, Y.-H. & Mackenzie, F. T. Changes in surface morphology of calcite exposed to the oceanic water column. *Aquat. Geochem.* **3**, 1–20 (1997).
36. Betzer, P. R. et al. The oceanic carbonate system: a reassessment of biogenic controls. *Science* **226**, 1074–1077 (1984).
37. Broecker, W. S. & Peng, T. H. *Tracers in the Sea* (Lamont-Doherty Geological Observatory, 1982).
38. Friis, K., Najjar, R. G., Follows, M. J. & Dutkiewicz, S. Possible overestimation of shallow-depth calcium carbonate dissolution in the ocean. *Glob. Biogeochem. Cycles* https://doi.org/10.1029/2006gb002727 (2006).
39. Jahnke, R. A. The global ocean flux of particulate organic carbon: areal distribution and magnitude. *Glob. Biogeochem. Cycles* **10**, 71–88 (1996).
40. Jenkins, C. J. Building offshore soils databases. *Sea Technol.* **38**, 25–28 (1997).
41. Honjo, S. Coccoliths: production, transportation and sedimentation. *Mar. Micropaleontol.* **1**, 65–79 (1976).
42. Subhas, A. V. et al. The dissolution behavior of biogenic calcites in seawater and a possible role for magnesium and organic carbon. *Mar. Chem.* **205**, 100–112 (2018).
43. Byrne, R. H., Acker, J. G., Betzer, P. R., Feely, R. A. & Cates, M. H. Water column dissolution of aragonite in the Pacific Ocean. *Nature* **312**, 321–326 (1984).
44. Boeuf, D. et al. Biological composition and microbial dynamics of sinking particulate organic matter at abyssal depths in the oligotrophic open ocean. *Proc. Natl Acad. Sci. USA* **116**, 11824–11832 (2019).
45. Haine, T. W. N. & Hall, T. M. A generalized transport theory: water-mass composition and age. *J. Phys. Oceanogr.* **32** (2002).
46. Bednaršek, N., Možina, J., Vogt, M., O'Brien, C. & Tarling, G. A. The global distribution of pteropods and their contribution to carbonate and carbon biomass in the modern ocean. *Earth Syst. Sci. Data* **4**, 167–186 (2012).
47. De La Rocha, C. L. & Passow, U. Factors influencing the sinking of POC and the efficiency of the biological carbon pump. *Deep Sea Res. II* **54**, 639–658 (2007).
48. Gehlen, M. et al. The fate of pelagic CaCO₃ production in a high CO₂ ocean: a model study. *Biogeosciences* **4**, 505–519 (2007).
49. Middelburg, J. J., Soetaert, K. & Hagens, M. Ocean alkalinity, buffering and biogeochemical processes. *Rev. Geophys.* https://doi.org/10.1029/2019RG000681 (2020).
50. Boucher, O., Denvil, S., Caubel, A. & Foujols, M. A. *IPSL-CM6A-LR Model Output Prepared for CMIP6 CMIP* Version 20200710 (Earth System Grid Federation, 2018); https://doi.org/10.22033/ESGF/CMIP6.1534
51. Boucher, O. et al. Presentation and evaluation of the IPSL-CM6A-LR climate model. *J. Adv. Model. Earth Syst.* https://doi.org/10.1029/2019ms002010 (2020).
52. Aumont, O., Ethé, C., Tagliabue, A., Bopp, L. & Gehlen, M. PISCES-v2: an ocean biogeochemical model for carbon and ecosystem studies. *Geosci. Model Dev.* **8**, 2465–2513 (2015).
53. Perez, F. F. et al. Meridional overturning circulation conveys fast acidification to the deep Atlantic Ocean. *Nature* **554**, 515–518 (2018).
54. Orr, J. C. et al. Anthropogenic ocean acidification over the twenty-first century and its impact on calcifying organisms. *Nature* **437**, 681–686 (2005).
55. Archer, D. Modeling the calcite lysocline. *J. Geophys. Res.* https://doi.org/10.1029/91jc01812 (1991).

Methods

This section presents the methodology to obtain the regional profiles of pelagic $CaCO_3$ dissolution and settling fluxes. For ease and clarity of instruction, steps taken in three regions of the Atlantic Ocean are graphically represented in Extended Data Figs. 1–6.

Seawater excess alkalinity. Carter et al.[56] introduced a tracer denoted Alk*, which uses the potential alkalinity concept of Brewer et al.[57] to remove the influence of organic matter cycling and a salinity normalization to remove the influence of freshwater cycling. Hence, Alk* has a global distribution determined primarily by $CaCO_3$ dissolution and precipitation[56]. Here we calculate the Alk* tracer using quality-controlled GLODAPv2[58,59] from the 2016 version, as per[56]:

$$Alk^* = TA + 1.26 \times \left[NO_3^-\right] - 66.4 \times S \tag{1}$$

where TA is titration alkalinity, 1.26 is an empirical ratio to account for the contributions from organic phosphorus and sulfur[60], $[NO_3^-]$ is the nitrate concentration and S is salinity. For GLODAPv2 samples in which TA was not measured, but with pH and dissolved inorganic carbon concentration measurements available, TA was computed using the MATLAB version of the CO2SYS algorithm[61,62] on the basis of in situ pH, dissolved inorganic carbon concentration, temperature, S, dissolved inorganic silica concentration and soluble reactive phosphate concentrations using the carbonic acid dissociation constants from Lueker et al.[63], the HSO_4^- dissociation constant from Dickson[64], the HF dissociation constant from Dickson and Riley[65], the boron-to-salinity ratio of Uppström[66] and the $B(OH)_3$ dissociation constant from Dickson[67]. Worldwide, 327,213 Alk* values were gathered, more than 98% from direct TA measurements. As in Carter et al.[56], Alk* was higher in the Pacific than in the Atlantic, with values ranging between 100 and 175 μmol kg^{-1} in most Pacific deep waters and between 50 and 100 μmol kg^{-1} in most Atlantic deep waters (Extended Data Fig. 1a). Negative Alk* values were observed at the ocean surface; they are the imprint left by net calcification but are uncertain due to freshwater cycling corrections.

Seawater age. The age of seawater (Extended Data Fig. 1b) was obtained using the TTD method approach applied on measured GLODAPv2 CFC-12 concentrations. Note that this is different from earlier studies on calcite dissolution[29–32] that used the tracer-age method, which potentially might induce bias. More background on the differences between the TTD method and the traditional tracer-age method is given in the Supplementary Information. For the age calculations, we assumed a balance between advective and diffusive mixing processes, defined as a ratio of the width and the mean age of the TTD equal to 1, which is a commonly applied assumption[68,69], and that CFC-12 was in full equilibrium with the atmosphere when leaving the surface ocean. While CFC-12 is a very useful tracer for most of the water column, the lower concentrations in old deep waters give a much larger uncertainty in the assessed ages. For these old waters, ^{14}C is a much preferred tracer[70]. Hence, for samples with CFC-12 TTD ages greater than 300 years, we used instead the seawater 'mean age' from Gebbie and Huybers[71], who applied an inverse modelling technique on GLODAP ^{14}C data[72]. The ^{14}C-derived age dataset of Gebbie and Huybers[71] was linearly interpolated in three dimensions to match the coordinates of the GLODAPv2 samples for which a CFC age was available. To avoid an abrupt transition between CFC-12 TTD ages and ^{14}C mean ages, for samples with TTD ages between 200 and 300 years, a transition function was applied to compute ages as a weighted average between the CFC-12 TTD ages and ^{14}C mean ages, that is, a mixture of the two age estimates. For all water masses younger than 200 years, we have used the CFC-12 TTD ages. We set the overall relative uncertainty associated with seawater ages to 20%, which should encompass both the uncertainty associated with the TTD method reported by He et al.[73] and the uncertainty associated with ^{14}C mean ages[71], neglecting the influence of exotic waters such as from groundwater seepage, hydrothermal vents or ice sheets[71].

Regionalization. Grouping data by region is required to perform the Alk*-age fits and derive pelagic $CaCO_3$ dissolution rates because our approach uses the accumulation rate of excess alkalinity along isopycnals as a proxy for $CaCO_3$ dissolution; hence, a high number of laterally distributed data points is needed for each dissolution-rate estimate. Here we have used the global open-ocean core biome distribution of Fay and McKinley[74], which is defined on the basis of sea surface temperature, chlorophyll a concentration, sea-ice fraction and maximum mixed-layer depth criteria. Thus, the regions considered for the present analysis are distinguished on the basis of ocean surface biogeochemical functions rather than water masses or topography. This is appropriate as the present study analyses the fate of biogenic particles sinking from the ocean surface. Note that when grouping data by region, there is a trade-off between increasing the geographical resolution of the $CaCO_3$ flux estimates by selecting small regions and increasing the statistical robustness of the estimates by selecting large regions with more seawater samples. To avoid facing the issue of under-sampled, narrow regions, we merged four biome pairs as defined by Fay and McKinley[74] into four distinct regions: the equatorial Pacific east and west, the subpolar and the subtropical seasonally stratified North Pacific, the subpolar and the subtropical seasonally stratified North Atlantic, and the subpolar and the subtropical seasonally stratified Southern Ocean. We also

excluded the Arctic and southernmost biomes, which are seasonally covered by sea ice, due to a lack of seawater chemistry data. Thus, we base our analysis on ten biogeochemically distinct regions, shown in Extended Data Fig. 2.

Dissolution-rate depth profiles. For each region, Alk* and age data were sorted according to increasing water potential density (σ_0, referenced to the surface, Extended Data Fig. 1c) and placed into bins centred around predefined σ_0 values; these bins constitute the isopycnals. The density bins spanned a broad density range, from $\sigma_0 = 24$ to $\sigma_0 = 28$, and were separated by a σ_0 increment kept constant over the entire σ_0 range. For each density bin, we performed a linear fit of Alk* versus seawater age and extracted the slope, mean depth and associated standard deviations (Extended Data Fig. 3). The slope of the Alk*-age linear relationship divided by 2 gives the r_{CaCO_3}, expressed in micromoles per kg per year, as for every mole of $CaCO_3$ dissolved, two moles of Alk* are released into seawater. To maximize statistical robustness, only fits performed on at least ten Alk* and age measurements, within which the age range was at least twice as large as the bin-averaged, overall relative age uncertainty (20%, see Uncertainty propagation), and the Alk* range was at least twice as large as the Alk* overall uncertainty (6 μmol kg^{-1}, see Uncertainty propagation) were retained to compute $CaCO_3$ dissolution rates.

We used a Monte Carlo approach to propagate uncertainties stemming from seawater age, Alk* and the definition of what constitutes an isopycnal to the final dissolution-rate estimates (explained in detail in Uncertainty propagation). Between each Monte Carlo simulation, the σ_0 increment randomly varied between 0.002 and 0.05, which made the isopycnals thinner or thicker, respectively, affecting the amount of data points on which each dissolution-rate estimate is based and the vertical extent of the reconstructed profiles. Consequently, for each Monte Carlo simulation, $CaCO_3$ dissolution rates were obtained at different mean water-column depths. To turn discrete $CaCO_3$ dissolution-rate profiles into continuous profiles, and allow comparison between each Monte Carlo simulation, $CaCO_3$ dissolution rates were interpolated over the entire depth range for which dissolution rates were available (Extended Data Fig. 4). For interpolation, a cubic smoothing spline function was applied to the dissolution-rate profiles, using a smoothing parameter $p = 5 \times 10^{-9}$ (ref. [75]), assigning to each dissolution-rate value a weight corresponding to the number of data points from which the dissolution rates were calculated. For example, for the same mean depth, a dissolution rate calculated from 100 Alk*-age data points will weight twice as much as a dissolution rate calculated from 50 data points in the spline smoothing process.

$CaCO_3$ flux to the seafloor. When reaching the seafloor, $CaCO_3$ dissolves in surface sediments and, for the remaining fraction that escapes early diagenesis, is buried in sediments. Here, we consider the $CaCO_3$ flux depositing to the seafloor to be the sum of the $CaCO_3$ burial rate in sediments and the $CaCO_3$ dissolution rate at the interface. An ocean-wide compilation of total sediment burial rates has been published before[39], but the corresponding $CaCO_3$ burial rates are unknown. Here, we used the total sediment burial rate dataset of Jahnke[39] and the $CaCO_3$ content of marine sediments extracted from the dbSEABED database of Jenkins[40], which have been quality controlled and harmonized into a homogeneous set of values[76]. $CaCO_3$ burial rates were computed by multiplying the total sediment burial rates by the $CaCO_3$ weight fraction in dry sediments. The resulting $1° \times 1°$ distribution of $CaCO_3$ burial rates is shown in Extended Data Fig. 5a. The $1° \times 1°$ distribution of the current total $CaCO_3$ dissolution rates at the seafloor was taken from Sulpis et al.[18] and is shown in Extended Data Fig. 5b. As for the dissolution-rate depth profiles, cubic smoothing spline functions were applied to the $CaCO_3$ burial and seafloor dissolution-rate datasets to turn $1° \times 1°$ distributions into regional, one-dimensional, continuous depth profiles. We set the overall relative uncertainty associated with $CaCO_3$ fluxes to the seafloor to 30%, which corresponds to the uncertainty associated with the estimate of global $CaCO_3$ dissolution rate at seafloor from Sulpis et al.[18], encompassing both seawater measurement and mapping error. No uncertainty was available for the $CaCO_3$ burial rates.

Settling flux reconstruction. The F_{CaCO_3} was then reconstructed assuming it balances all dissolution occurring in the depth level directly underneath it (Extended Data Fig. 6). At depth horizon z, the flux is therefore given by

$$F_{CaCO_3}(z) = \int_{z_{deepest}}^{z} r_{CaCO_3}\, dz + F_{CaCO_3}(z_{deepest}), \tag{2}$$

where $z_{deepest}$ corresponds to the depth of the deepest $CaCO_3$ dissolution-rate estimate for a given region and a given Monte Carlo simulation, and $F_{CaCO_3}(z_{deepest})$ is the $CaCO_3$ flux to the seafloor at a water depth corresponding to $z_{deepest}$, obtained as explained in the '$CaCO_3$ flux to the seafloor' section. We assume that the horizontal transport of settling $CaCO_3$ particles is negligible compared with their vertical sinking, which is an acceptable assumption given mean settling velocities higher than 10 m d^{-1} in the pelagic ocean[77–79].

The upper limit of the reconstructed F_{CaCO_3} profiles corresponds to the shallowest depth for which r_{CaCO_3} estimates are available. For consistency between profiles from each Monte Carlo simulation, we set this limit to 300 m, which is also beneath the euphotic zone and beneath the mixed layer over all latitudes[80,81], hence a more appropriate reference depth than the ocean surface to represent biogenic particle settling fluxes[82].

Uncertainty propagation. We quantified the uncertainties around our r_{CaCO_3} and F_{CaCO_3} estimates by propagating various sources of uncertainty using a Monte Carlo approach. For r_{CaCO_3}, uncertainty can originate from the seawater Alk* estimates, the seawater age estimates or the definition of what constitute isopycnals for which dissolution rates are calculated. For F_{CaCO_3}, uncertainty can originate from the r_{CaCO_3} estimates and from uncertainties associated with estimates of the $CaCO_3$ flux to the seafloor. Hence, each Monte Carlo calculation proceeded as follows:

1. Seawater Alk* was computed from GLODAPv2 data according to equation (1). Each Alk* estimate was altered by a randomly generated value between −6 and +6 µmol kg⁻¹, which corresponds to the overall uncertainty associated with GLODAPv2 TA measurements[59].

2. Seawater ages, obtained as explained in the 'Seawater age' section, were altered by a randomly generated value between −20% and +20% of the initial age, taking 20% as an overall relative uncertainty (see the 'Seawater age' section).

3. In each region, seawater potential density (σ_0) bins were generated, and the σ_0 increment that separates each bin was assigned a randomly chosen value between $\sigma_0 = 0.002$ and $\sigma_0 = 0.05$. Dissolution rates were calculated in each bin, and continuous dissolution-rate depth profiles were generated as explained in the 'Dissolution-rate depth profiles' section.

4. $CaCO_3$ fluxes to the seafloor were obtained as explained in the '$CaCO_3$ flux to the seafloor' section. Each 1° × 1° grid estimate of the $CaCO_3$ flux to the seafloor was altered by a randomly generated value between −30% and +30% of the initial flux, which corresponds to the overall uncertainty associated with the $CaCO_3$ fluxes to the seafloor (see the '$CaCO_3$ flux to the seafloor' section).

5. Regional mean F_{CaCO_3} depth profiles were then reconstructed, as explained in the 'Settling flux reconstruction' section.

This procedure was repeated 10,000 times, providing 10,000 independent r_{CaCO_3} and F_{CaCO_3} depth profiles for each region. From these 10,000 depth profiles, we computed the mean r_{CaCO_3} and F_{CaCO_3} depth profiles for each region, and we used 90% confidence intervals and standard deviations to place uncertainty bounds.

Comparison with sediment-trap data. The reconstructed $CaCO_3$ settling fluxes were compared with $CaCO_3$ flux measurements originating from the sediment-trap dataset of Mouw et al.[83]. Locations of the sediment-trap data that were used are shown in the central map of Extended Data Fig. 2. Sediment-trap data from the same location and depth were averaged over time to eliminate short-term variability and the effects of seasonality. In total, 229 sediment-trap $CaCO_3$ settling fluxes were gathered in the ten regions on which this study focuses, covering a depth range from 50 metres to 5,090 metres beneath the sea surface, with an average sediment-trap sampling duration of 109 days. These sediment-trap observations were used to assess the accuracy of our regional $CaCO_3$ settling fluxes and those from other sources (Supplementary Information).

$CaCO_3$ saturation depths. To visualize the $CaCO_3$-dissolution depth profiles in each biome with relevant water-column biogeochemical markers, we computed biome-averaged aragonite and calcite saturation depths from the GLODAPv2 dataset. Using the MATLAB version of the CO2SYS software[61,62], on the basis of in situ pH, TA, temperature, S, dissolved inorganic silica concentration and soluble reactive phosphate concentrations, using the carbonic acid dissociation constants from Lueker et al.[63], the HSO_4^- dissociation constant from Dickson[64], the HF dissociation constant from Dickson and Riley[65], the boron-to-salinity ratio of Uppström[66] and the $B(OH)_3$ dissociation constant from Dickson[67], we extracted for each GLODAPv2 sample the saturation states of seawater with respect to calcite and aragonite, denoted Ω_C and Ω_A, respectively, and the seawater $[CO_3^{2-}]$. We also calculated seawater $[Ca^{2+}]$ from S[84]. Dividing the seawater $[CO_3^{2-}] \times [Ca^{2+}]$ concentration product by the typical stoichiometry solubility product of Mg calcites secreted by fish ($pK_{sp}^* = 5.89 \pm 0.09$)[4], we derived the saturation state of seawater with respect to Mg calcites, denoted Ω_{Mg-C}. For each region, the arithmetic averages of water-column depths associated with data points with $0.95 \leq \Omega_C \leq 1.05$, $0.95 \leq \Omega_A \leq 1.05$ and $0.95 \leq \Omega_{Mg-C} \leq 1.05$ were considered to be the biome-averaged calcite, aragonite and Mg-calcite saturation depths, respectively. For each of these three horizons, the standard deviation associated with the depth averages was considered to be representative of the overall uncertainty.

Data availability

The TTD ages[85] are made available as GLODAPv2 affiliated data on the NOAA Ocean Carbon Data System website at https://www.ncei.noaa.gov/access/ocean-carbon-data-system/oceans/ndp_108/ndp108.html. Seawater chemistry data are available from the GLODAPv2.2016 in refs. [58,59], sediment-trap data are available from ref. [83], ¹⁴C-derived ages are available from ref. [71], biome distributions are available from ref. [74] and sediment fluxes are available from refs. [18,39,40].

Code availability

The MATLAB script to reproduce the regional $CaCO_3$ dissolution rate and reconstructed settling fluxes is available at https://github.com/osulpis/pelagic_dissolution.

References

56. Carter, B. R., Toggweiler, J. R., Key, R. M. & Sarmiento, J. L. Processes determining the marine alkalinity and calcium carbonate saturation state distributions. *Biogeosciences* **11**, 7349–7362 (2014).

57. Brewer, P. G., Wong, G. T. F., Bacon, M. P. & Spencer, D. W. An oceanic calcium problem? *Earth Planet. Sci. Lett.* **26**, 81–87 (1975).

58. Key, R. M. et al. *Global Ocean Data Analysis Project* Version 2 (GLODAPv2), ORNL/CDIAC-162, NDP-P093 (DOE, 2015).

59. Olsen, A. et al. The Global Ocean Data Analysis Project version 2 (GLODAPv2)—an internally consistent data product for the world ocean. *Earth Syst. Sci. Data* **8**, 297–323 (2016).

60. Kanamori, S. & Ikegami, H. Calcium-alkalinity relationship in the North Pacific. *J. Oceanogr. Soc. Jpn* **38**, 57–62 (1982).

61. MS Excel Program Developed for CO_2 System Calculations (ORNL/CDIAC-105a) (DOE, 2006).

62. van Heuven, S., Pierrot, D., Rae, J. W. B., Lewis, E. & Wallace, D. W. R. MATLAB Program Developed for CO_2 System Calculations (ORNL/CDIAC-105b) (DOE, 2011); https://doi.org/10.3334/CDIAC/otg.CO2SYS_MATLAB_v1.1

63. Lueker, T. J., Dickson, A. G. & Keeling, C. D. Ocean pCO_2 calculated from dissolved inorganic carbon, alkalinity, and equations for K_1 and K_2: validation based on laboratory measurements of CO_2 in gas and seawater at equilibrium. *Mar. Chem.* **70**, 105–119 (2000).

64. Dickson, A. G. Standard potential of the reaction: $AgCl(s) + 1/2H_2(g) = Ag(s) + HCl(aq)$, and the standard acidity constant of the ion HSO_4^- in synthetic seawater from 273.15 to 318.15 K. *J. Chem. Thermodyn.* **22**, 113–127 (1990).

65. Dickson, A. G. & Riley, J. P. The estimation of acid dissociation constants in seawater media from potentionmetric titrations with strong base. I. The ionic product of water—K_w. *Mar. Chem.* **7**, 89–99 (1979).

66. Uppström, L. R. The boron/chlorinity ratio of deep-sea water from the Pacific Ocean. *Deep Sea Res. Oceanogr. Abstr.* **21**, 161–162 (1974).

67. Dickson, A. G. Thermodynamics of the dissociation of boric acid in synthetic seawater from 273.15 to 318.15 K. *Deep Sea Res. A* **37**, 755–766 (1990).

68. Waugh, D. W., Haine, T. W. N. & Hall, T. M. Transport times and anthropogenic carbon in the subpolar North Atlantic Ocean. *Deep Sea Res. I* **51**, 1475–1491 (2004).

69. Waugh, D. W., Hall, T. M., McNeil, B. I., Key, R. & Matear, R. J. Anthropogenic CO_2 in the oceans estimated using transit time distributions. *Tellus B* **58**, 376–389 (2006).

70. Stöven, T., Tanhua, T., Hoppema, M. & Bullister, J. L. Perspectives of transient tracer applications and limiting cases. *Ocean Sci.* **11**, 699–718 (2015).

71. Gebbie, G. & Huybers, P. The mean age of ocean waters inferred from radiocarbon observations: sensitivity to surface sources and accounting for mixing histories. *J. Phys. Oceanogr.* **42**, 291–305 (2012).

72. Key, R. M. et al. A global ocean carbon climatology: results from Global Data Analysis Project (GLODAP). *Glob. Biogeochem. Cycles* https://doi.org/10.1029/2004gb002247 (2004).

73. He, Y.-C. et al. A model-based evaluation of the inverse Gaussian transit-time distribution method for inferring anthropogenic carbon storage in the ocean. *J. Geophys. Res. Oceans* **123**, 1777–1800 (2018).

74. Fay, A. R. & McKinley, G. A. Global open-ocean biomes: mean and temporal variability. *Earth Syst. Sci. Data* **6**, 273–284 (2014).

75. De Boor, C. *A Practical Guide to Splines* Vol. 27 (Springer-Verlag, 1978).

76. Goff, J. A., Jenkins, C. J. & Williams, S. J. Seabed mapping and characterization of sediment variability using the usSEABED data base. *Cont. Shelf Res.* **28**, 614–633 (2008).

77. Hemleben, C., Spindler, M. & Anderson, O. R. *Modern Planktonic Foraminifera* (Springer-Verlag, 1989).

78. Noji, T. T. et al. Clearance of picoplankton-sized partides and formation of rapidly sinking aggregates by the pteropod, *Limacina reiroversa*. *J. Plankton Res.* **19**, 863–875 (1997).

79. Berelson, W. M. Particle settling rates increase with depth in the ocean. *Deep Sea Res. II* **49**, 237–251 (2001).

80. Weber, T., Cram, J. A., Leung, S. W., DeVries, T. & Deutsch, C. Deep ocean nutrients imply large latitudinal variation in particle transfer efficiency. *Proc. Natl Acad. Sci. USA* **113**, 8606–8611 (2016).

81. Morel, A. et al. Examining the consistency of products derived from various ocean color sensors in open ocean (Case 1) waters in the perspective of a multi-sensor approach. *Remote Sens. Environ.* **111**, 69–88 (2007).

82. Buesseler, K. O., Boyd, P. W., Black, E. E. & Siegel, D. A. Metrics that matter for assessing the ocean biological carbon pump. *Proc. Natl Acad. Sci. USA* **117**, 9679–9687 (2020).

83. Mouw, C. B., Barnett, A., McKinley, G. A., Gloege, L. & Pilcher, D. Global ocean particulate organic carbon flux merged with satellite parameters. *Earth Syst. Sci. Data* **8**, 531–541 (2016).

84. Riley, J. P. & Tongudai, M. The major cation/chlorinity ratios in sea water. *Chem. Geol.* **2**, 263–269 (1967).

85. Jeansson, E., Steinfeldt, R. & Tanhua, T. *Water Mass Ages Based On GLODAPv2 Data Product (NCEI Accession 0226793)* (NOAA, National Centers for Environmental Information, 2021).

Author contributions

O.S. and J.J.M. designed the research. O.S. performed the data analysis with inputs from A.D. and wrote the manuscript with contributions from all authors. E.J. and S.K.L. contributed the TTD-age analysis and advised on its usage. All authors interpreted the results and edited the manuscript.

Competing interests

The authors declare no competing interests.

Additional information

Extended data is available for this paper at https://doi.org/10.1038/s41561-021-00743-y.

Supplementary information The online version contains supplementary material available at https://doi.org/10.1038/s41561-021-00743-y.

Correspondence and requests for materials should be addressed to O.S.

Peer review information *Nature Geoscience* thanks Andreas Andersson, Kai Schulz and the other, anonymous, reviewer(s) for their contribution to the peer review of this work. Primary Handling Editor: Xujia Jiang.

**Reprints and permissions information** is available at www.nature.com/reprints.
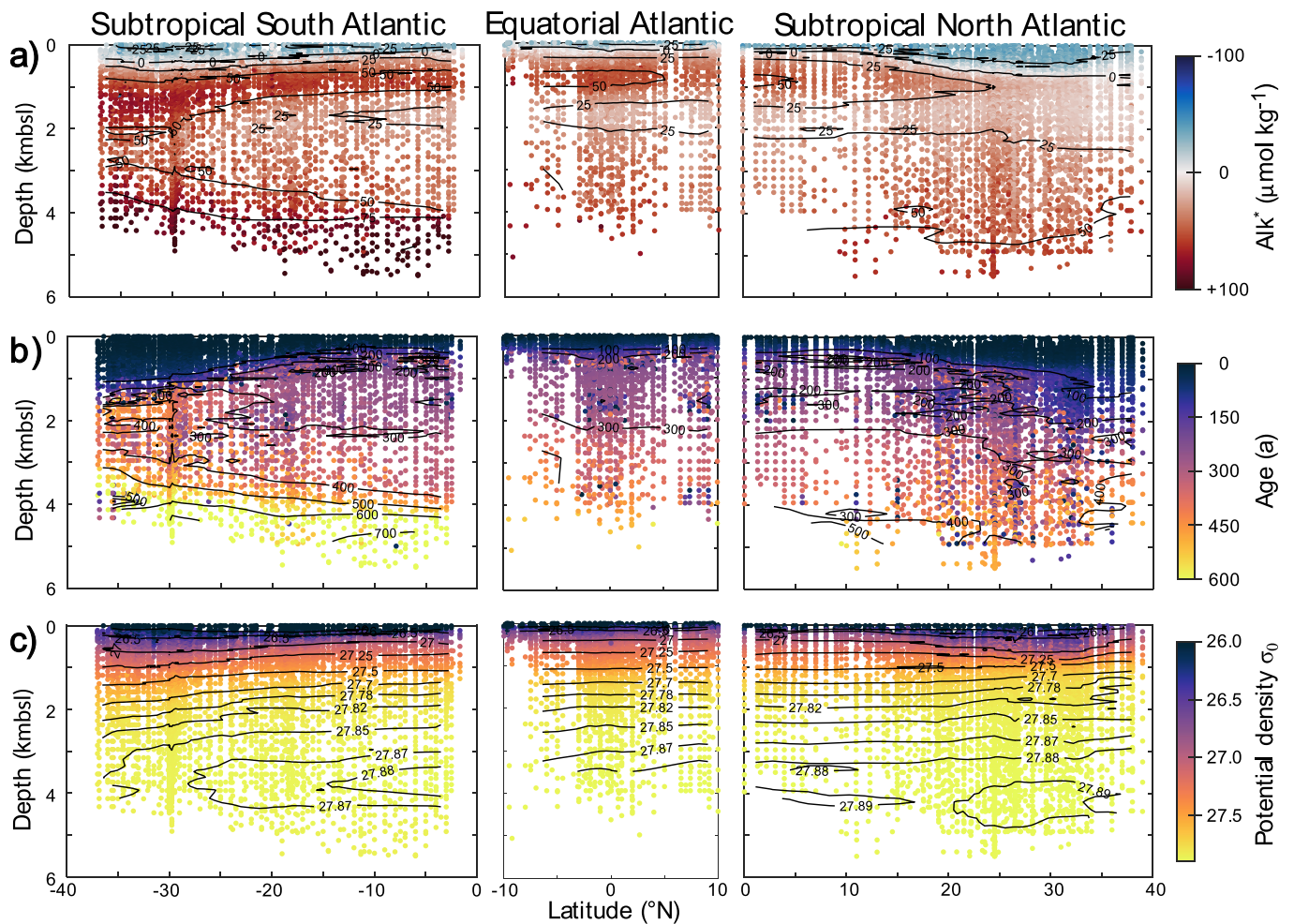
Extended Data Fig. 1 | Depth-latitude distributions of seawater properties in the Atlantic Ocean. a, Seawater Alk*, **b,** seawater age and **c,** potential density (σ_0) are shown in depth-latitude diagrams separated according to three biogeochemically-distinct regions on which we base our analysis, corresponding to the (**left**) subtropical South Atlantic, (**center**) Equatorial Atlantic and (**right**) subtropical Noth Atlantic regions shown in Extended Data Fig. 2.
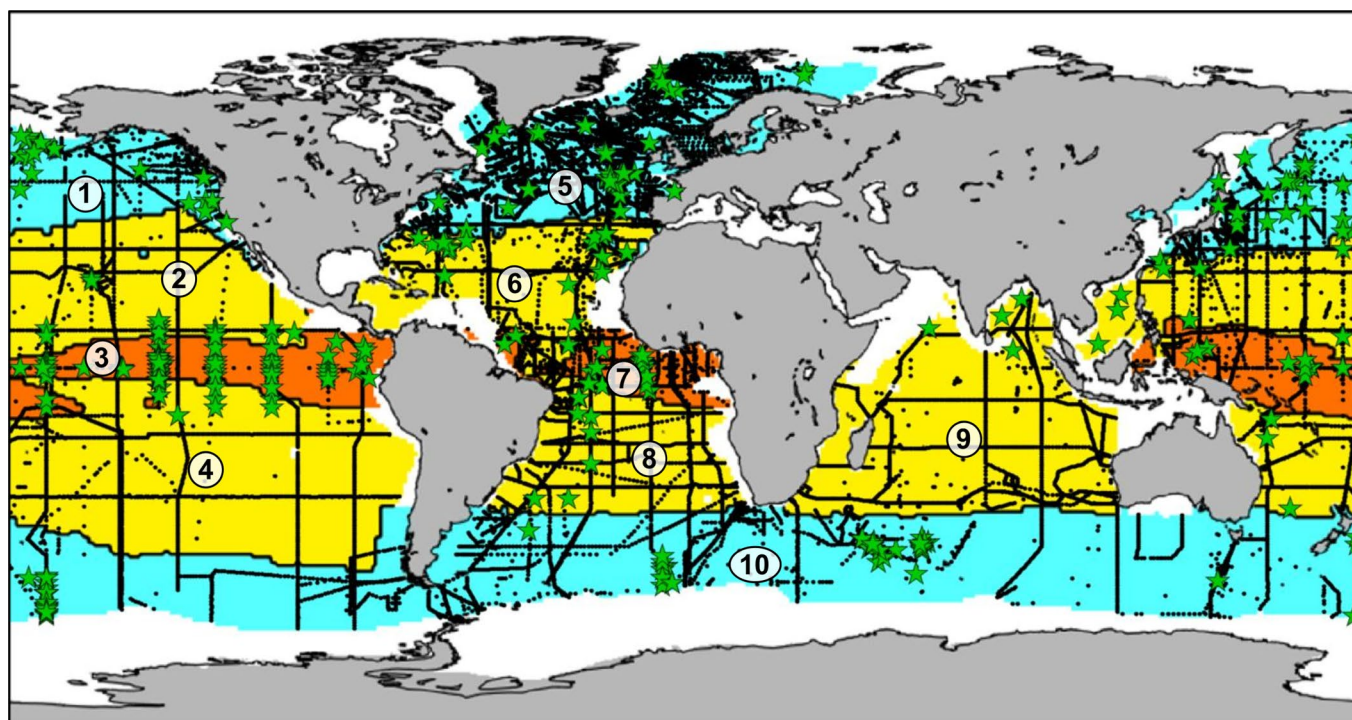
Extended Data Fig. 2 | Oceanic regions. Geographical boundaries of the 10 regions used for our study. Black dots correspond to the locations of GLODAPv2 seawater chemistry and age data. Green stars correspond to the locations of sediment-trap data. The numbers indicate the 10 regions: **1**, subpolar North Pacific, **2**, subtropical North Pacific, **3**, Equatorial Pacific, **4**, subtropical South Pacific, **5**, subpolar North Atlantic, **6**, subtropical North Atlantic, **7**, Equatorial Atlantic, **8**, subtropical South Atlantic, **9**, Indian Ocean and **10**, Southern Ocean. Polar regions are in blue, subtropical regions are in yellow and equatorial regions are in orange.
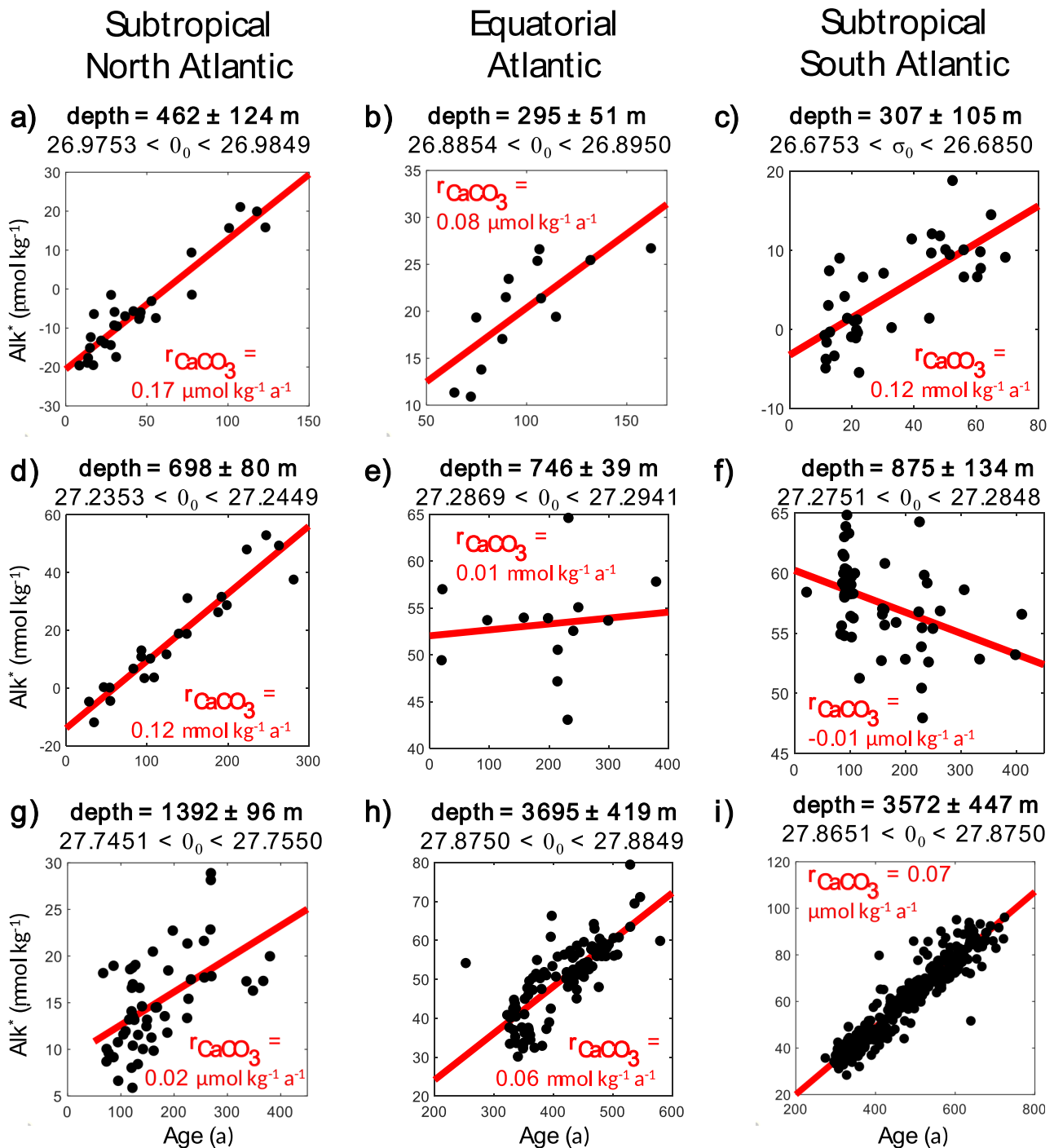
Extended Data Fig. 3 | Alk* versus seawater age plots from the Atlantic Ocean. Plots corresponding to randomly selected density bins from the Suptropical North Atlantic (**a,d,g**), Equatorial Atlantic (**b,e,h**) and Subtropical South Atlantic (**c,f,i**). The spatial distribution of the Alk* and seawater age data is shown in Extended Data Fig. 1. Red lines are linear fits from which $CaCO_3$ dissolution rates are estimated, computed as half of the slope, expressed in $\mu mol\ kg^{-1}\ a^{-1}$. For each regional density, the mean depth ($\pm 1\sigma$) and the σ_0 range are reported.
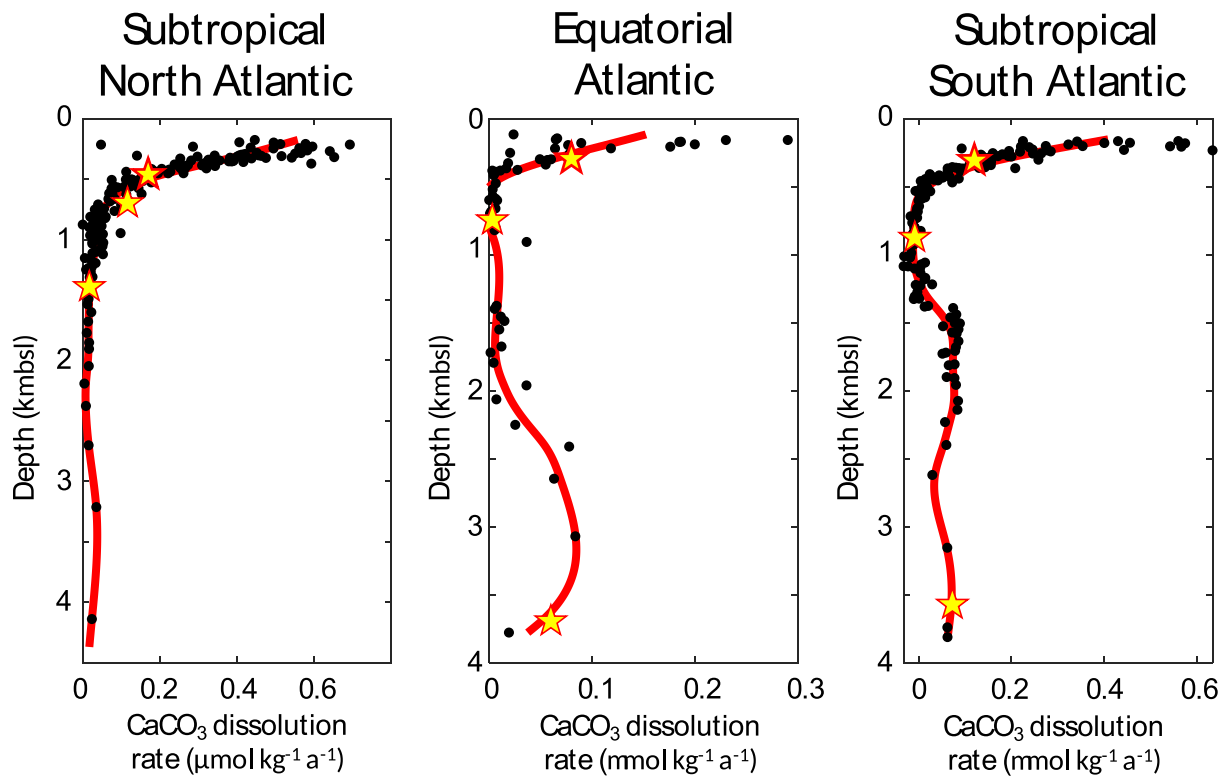
Extended Data Fig. 4 | CaCO$_3$ dissolution rate profiles from the Atlantic Ocean. Black points correspond to discrete CaCO$_3$ dissolution rate estimates computed as shown in Extended Data Fig. 3, using a constant sigma increment ($\sigma_0 = 0.01$). Yellow stars represent the 9 CaCO$_3$ dissolution rate estimates originating from Extended Data Fig. 3. Red lines are cubic smoothing splines used to interpolate discrete dissolution rate estimates over depth and obtain regionally harmonized depth profiles.
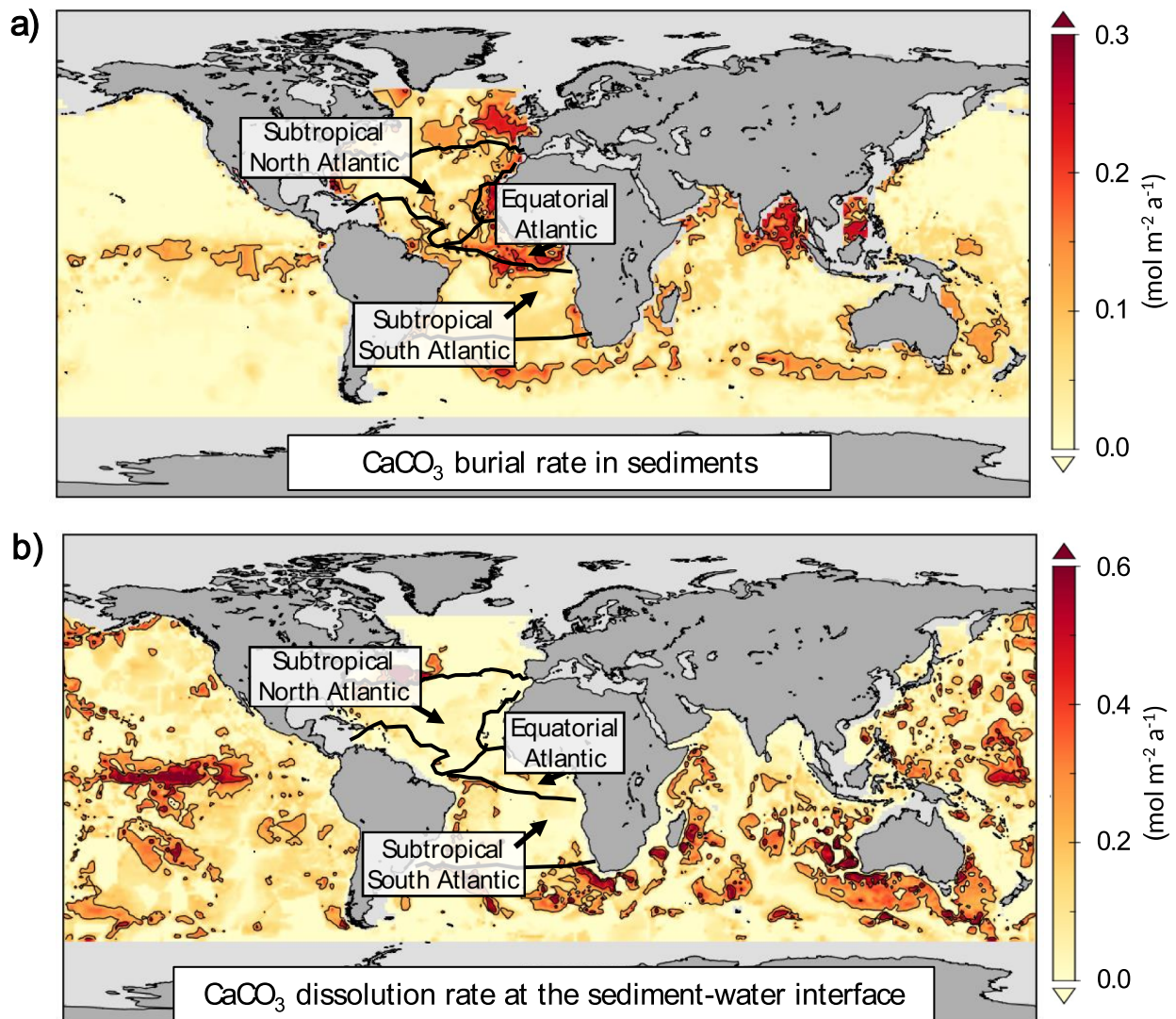
Extended Data Fig. 5 | CaCO₃ burial and dissolution rates at the seafloor. The sum of (**a**) the burial rate at the seafloor and (**b**) the dissolution rate at the sediment-water interface represents the CaCO₃ flux reaching the seafloor. The three Atlantic regions on which the *Methods* section focuses are contoured in a black thick line.
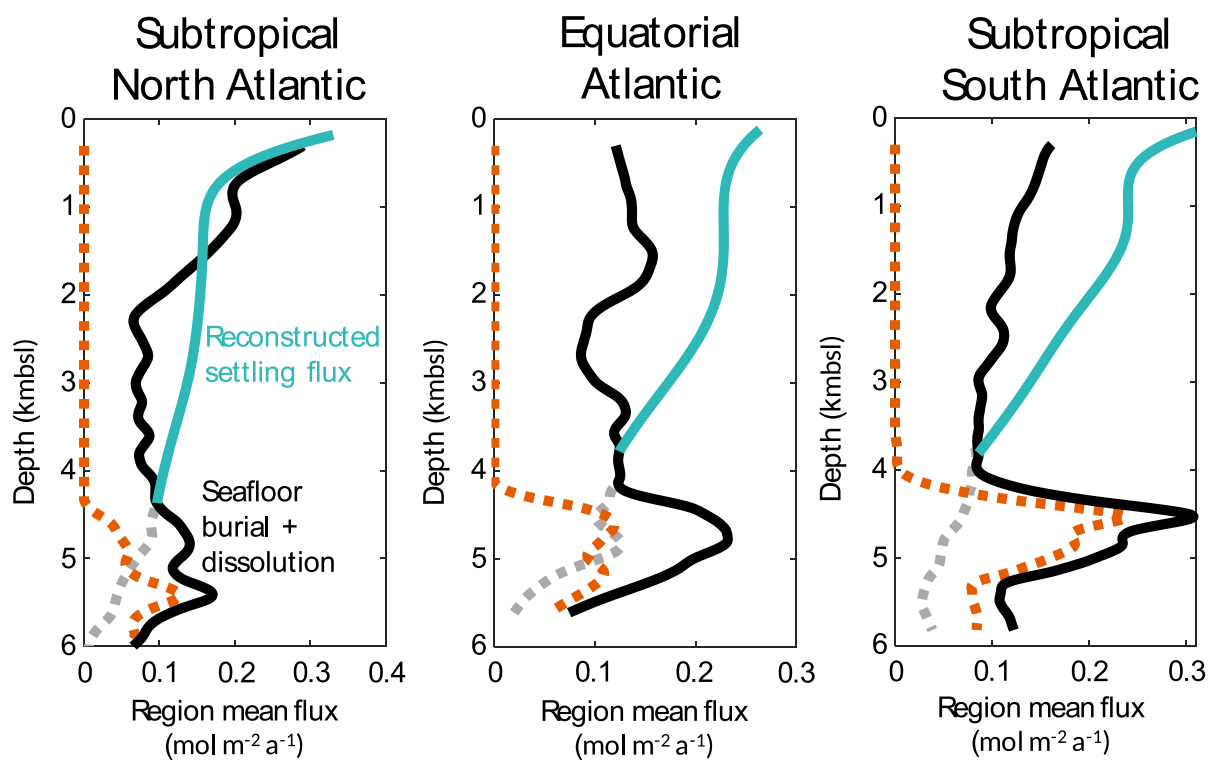
Extended Data Fig. 6 | Atlantic seafloor CaCO₃ sinks and reconstructed settling fluxes. In each panel, the orange dashed line represents the CaCO₃ dissolution rate at the sediment-water interface depth profile (from Extended Data Fig. 5a), the grey dashed line represents the CaCO₃ burial rate in sediments (from Extended Data Fig. 5b), the solid black line is the sum of seafloor dissolution and burial at each depth and the solid turquoise line is the reconstructed CaCO₃ settling flux.